

Active broadband unidirectional focusing of terahertz surface plasmons based on a liquid-crystal-integrated on-chip metadvice

YI-MING WANG,¹ FEI FAN,^{1,2,*} HUI-JUN ZHAO,¹ JING LIU,² YUN-YUN JI,²  JIE-RONG CHENG,¹ AND SHENG-JIANG CHANG²

¹Tianjin Key Laboratory of Micro-scale Optical Information Science and Technology, Institute of Modern Optics, Nankai University, Tianjin 300350, China

²Tianjin Key Laboratory of Optoelectronic Sensor and Sensing Network Technology, Tianjin 300350, China

*Corresponding author: fanfei@nankai.edu.cn

Received 16 April 2024; revised 14 July 2024; accepted 16 July 2024; posted 18 July 2024 (Doc. ID 527697); published 16 September 2024

Surface plasmons have been given high expectations in terahertz (THz) on-chip photonics with highly bound integrated transmission and on-chip wavefront engineering. However, most surface plasmonic coupling strategies with tailorable polarization-dependent features are challenged in broadband propagation and dynamic manipulation. In this work, a liquid crystal (LC)-integrated surface plasmonic metadvice based on arc-arrayed pair-slit resonators (APSRs) is demonstrated. The mirror-symmetry structures of this metadvice achieve the spin-selective unidirectional achromatic focusing, of which the broadband characteristic is supported by containing multiple APSRs with slits of different sizes corresponding to different excitation frequencies. Moreover, arc radii are precisely designed to meet the phase matching condition of constructive interference, so that the operating frequency of this on-chip metadvice is broadened to 0.33–0.60 THz. Furthermore, the LC integration provides the active energy distribution between the left and right focal spots, and the actual modulation depth reaches up to 73%. These THz active, wideband, on-chip manipulation mechanisms and their devices are of great significance for THz-integrated photonic communication, information processing, and highly sensitive sensing. © 2024 Chinese Laser Press

<https://doi.org/10.1364/PRJ.527697>

1. INTRODUCTION

With the rapid development of terahertz (THz) technology, THz functional devices provide critical support in the fields of wireless communications, high-resolution imaging, and biochemical sensing [1,2]. In particular, metasurfaces provide wide applications for free-space beam steering [3–5], but controlling on-chip propagation requires new mechanisms. Surface plasmons (SPs) are special electromagnetic modes propagating at the conductor-medium interface, showing great prospects in ultra-compact optical devices and integrated systems [6,7]. Unfortunately, in the THz regime, surface plasmonic waves (SPWs) at flat metal surfaces can hardly be highly confined. Structured metallic surfaces composed of subwavelength elements provide a way to construct on-chip metadvice, of which the resonance fields are capable of SP coupling and control [8,9]. In recent years, THz SPW-based devices have made great progress [10–12], meeting the requirements of miniaturization, low energy consumption, high efficiency, and on-chip integration in future THz applications.

Previous studies have shown that the excitation and propagation of SPWs are controllable by precisely customizing the geometry and distribution of microstructural units [13–15]. In 2013, Lin *et al.* utilized plasmonic hole array structures to realize the spin-dependent directional excitation of surface waves in the visible and near-infrared bands [16], which also provides a path for efficient generation and flexible wavefront control of SPWs in the THz band [17–19]. For example, based on the Pancharatnam–Berry mechanism, Wang *et al.* proposed a gradient-phase on-chip metadvice that converts the circularly polarized (CP) beams into SPWs with focusing or defocusing, dictated by the chirality of the incidences [19]. However, the on-chip wavefront manipulation of SPW typically requires complex shapes or several phase elements. The SPW interference effect of subwavelength slits offers an alternative route to simplify the design process [20–22]. In 2022, an SP metalens was constructed by two sets of slit pairs with different resonance responses as the basic unit, which can work for non-uniformly polarized incidence [20]. It is worth noting that, because of the

strong dispersion of SPWs, broadband wavefront manipulations for THz SPWs have been rarely reported [23,24], which hinders the development of broadband communication and optical information processing, especially about on-chip achromatic wavefront modulation.

Moreover, on-chip active manipulation of THz SPWs has also faced challenges, due to the difficulties in the functional material integration on-chip and the active interaction with THz waves [25–27]. The modulations of a unidirectional SPW launcher and propagator based on metadevices are almost passive, or simply by mechanically changing the incident polarization [28–30]. To our knowledge, there are few experimental reports on active THz SPW on-chip transmission or wavefront modulation [26,27,31]. The strategy of introducing functional materials into microstructures, such as semiconductors, graphene, and vanadium dioxide, has been widely applied in active metasurfaces to manipulate the free-space THz waves [32–34], which is of referential significance for the development of active THz SPW on-chip devices.

In particular, liquid crystal (LC) has broadband adjustable anisotropy in the THz regime, so remarkable phase shift and polarization conversion can be reversibly and continuously regulated by thermal, optical, electrical, and magnetic means [35–37]. There have been some works on free-space wavefront modulation based on THz LC metadevices, such as LC active beam deflection and coded metasurfaces [38–40]. Recently, Zhuang *et al.* demonstrated a metasurface with an LC elastomer as the substrate, enabling broadband wavefront steering by the control method of infrared light or heating [41]. Therefore, the combination with the LC configuration is considered a

promising method to develop active THz devices, but it has been rarely applied in SPW-based metadevices.

In this work, we take the lead in demonstrating the broadband focusing and the active modulation of on-chip SPWs. To achieve this purpose, an on-chip metadvice based on the combination of arc-arrayed pair-slit resonators (APSRs) and LC configuration is proposed. In our scheme, multiple APSRs with mirror symmetry are adopted to achieve spin-selective unidirectional focusing of SPWs. More importantly, the broadband feature is realized by selecting several slit geometric sizes and further considering the corresponding arc radius to meet the phase-matching conditions. Moreover, the integration of LC introduces an approach for the polarization conversion enabling SPW intensity modulation and dynamic energy distribution between left and right focal spots.

2. METHOD

A. Geometric Structure and Theoretical Analysis

Figure 1(a) schematically illustrates the principle of wideband excitation and unidirectional focusing of multi-APSRs for THz SPWs. This on-chip metadvice is a metallic thin film with a subwavelength pair-slit as its basic structure. Each APSR with the same central angle ψ is composed of ψ/θ pair-slits arrayed by the equal angular spacing θ . As shown in the detailed diagram in Fig. 1(a), one pair-slit consists of two slits of the same geometric size, with an orientation angle of $\phi_1 = 135^\circ$ and $\phi_2 = 45^\circ$. Their geometric centers with transverse and longitudinal relative distances l are both at $\lambda_{\text{SPW}}/4$. The excited SPW field under the CP incidence can be expressed as follows [16,42]:

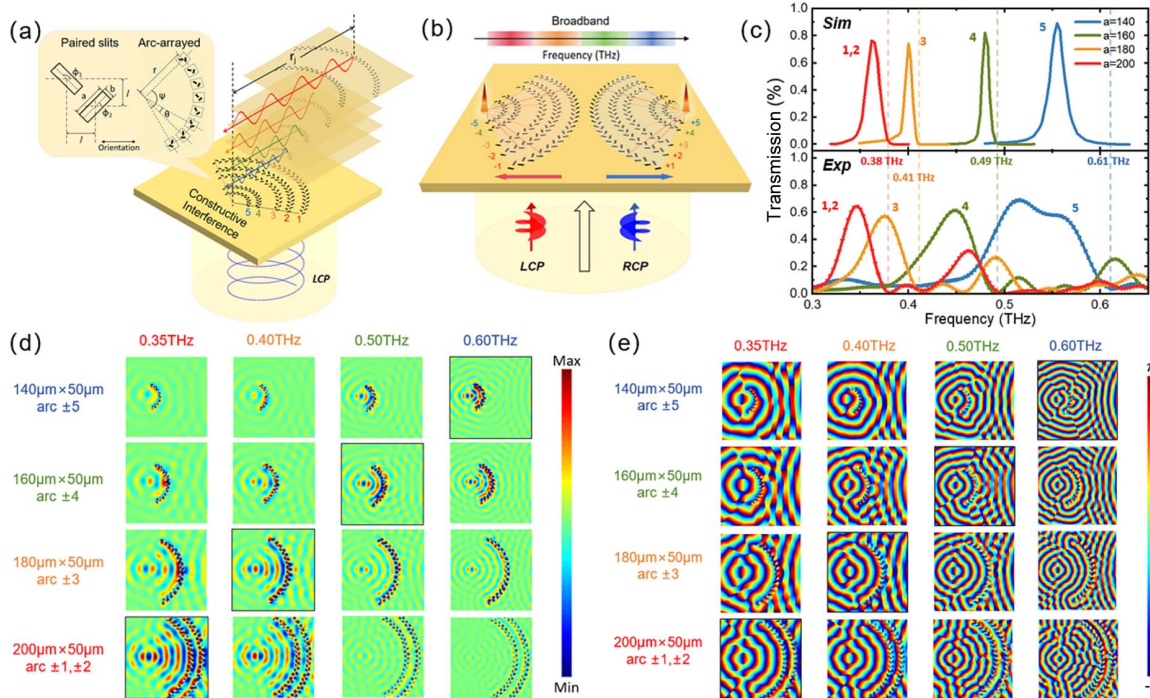


Fig. 1. (a) Schematic diagram of the broadband SPW excitation in the multi-APSR. Left corners are the detailed diagrams of paired slits and one single APSR structure. (b) Functions of broadband APSR. (c) Simulated and experimental transmission spectra of slits with different geometric sizes. (d) Simulated E_z near-field (real part) distribution and (e) phase maps of SPWs excited by each APSR at 0.35, 0.40, 0.50, and 0.60 THz.

$$E_{\tau,\sigma} = \frac{\tilde{C}}{\sqrt{2}l} \tau \left[e^{i\frac{\tilde{C}}{4}(\sigma+\tau)} + e^{-i\frac{\tilde{C}}{4}(\sigma+\tau)} \right], \quad (1)$$

where $\tau = -1$ and $+1$ respectively represent one-way excitation to the left and right sides of the pair-slit unit; $\sigma = -1$ and $+1$ represent right-handed circular polarization (RCP) and left-handed circular polarization (LCP) incidences. \tilde{C} is a complex coefficient determined by the response of SPWs on a single slit. It is indicated that the LCP/RCP incidence only excites the SPWs to the left/right along the unit orientation, which is called spin-dependent unidirectional excitation.

The wavefront shaping of SPWs can be realized by arranging the orientation of the pair-slits. As illustrated in Fig. 1(a), each arc-shaped structure is composed of pair-slits with the same geometry, which are arrayed in a radial orientation with an equal distance r to the center. In one APSR, the SPWs excited from each pair-slit can propagate radially towards the arc center with the same efficiency, forming a focal spot with strong intensity due to the same initial phase and propagation phase. In contrast, when the SPWs propagate radially outwards, the intensity is much weaker owing to the divergent wavefront and can hardly be detected. The on-chip metadvice is further designed as two sets of multi-APSRs with mirror symmetry as shown in Fig. 1(b). Each side of the structure consists of five concentric arcs with $\psi = 120^\circ$, which are numbered as $j = 1-5$ from the outermost to the innermost, with $+$ and $-$ representing the right side and left side, respectively. The APSR metadvice excites the SPWs unidirectionally focusing at the left/right center responding to LCP/RCP wave incidence.

As defined in Eq. (1), for a certain arc under the incident LCP (RCP) wave, the SPW will be excited unidirectionally toward the center with the initial SPW field obtained as $E_{1,-1} = \frac{\tilde{C}}{\sqrt{l/2}} (E_{-1,1} = -\frac{\tilde{C}}{\sqrt{l/2}})$. More importantly for the multi-APSRs, the overall SPW field is the interference between $E_{-1,1}$ from the different five arcs on the left side, while $E_{1,-1}$ in the right-side field. The SPW fields E_F at the left/right center are calculated by Eqs. (2) and (3):

$$\begin{aligned} E_{F,L} &= \sum_j -\frac{\tilde{C}_j}{\sqrt{l_j/2}} A_{\text{LCP}} e^{i[\phi_{\text{LCP}} - k_{\text{SPW}} \cdot (-r_j)]} \\ &= \sum_j -\frac{|C_j|}{\sqrt{l_j/2}} A_{\text{LCP}} e^{i[\phi_{\text{LCP}} + k_{\text{SPW}} \cdot r_j + \text{ang}(C_j)]}, \end{aligned} \quad (2)$$

$$\begin{aligned} E_{F,R} &= \sum_j +\frac{\tilde{C}_j}{\sqrt{l_j/2}} A_{\text{RCP}} e^{i(\phi_{\text{RCP}} + k_{\text{SPW}} \cdot r_j)} \\ &= \sum_j +\frac{|C_j|}{\sqrt{l_j/2}} A_{\text{RCP}} e^{i[\phi_{\text{RCP}} + k_{\text{SPW}} \cdot r_j + \text{ang}(C_j)]}. \end{aligned} \quad (3)$$

Neglecting the loss of divergent propagation from the other side, they can be uniformly described as Eq. (4):

$$E_F = \sum_j \tau A_\sigma \frac{|C_j|}{\sqrt{l_j/2}} e^{i[\phi_\sigma + k_{\text{SPW}} \cdot r_j + \text{ang}(C_j)]}, \quad (4)$$

where r_j represents the distance from the slit position to a certain on-chip point.

To ensure the SPW focuses from the different arcs simultaneously, constructive interference is desired to happen at the left/right center, of which conditions can be described as follows:

$$|C_{j+1}|/|C_j| = \sqrt{l_{j+1}/l_j} = \sqrt{\lambda_{\text{SPW},j+1}/\lambda_{\text{SPW},j}}, \quad (5)$$

$$k_{\text{SPW}}(r_{j+1} - r_j) + \text{ang}(C_{j+1}/C_j) = 2n\pi, \quad (6)$$

where n is an integer, and $k_{\text{SPW}} = 2\pi/\lambda_{\text{SPW}}$ is the wave vector with the SPW wavelength λ_{SPW} . In this case, Eq. (4) can be expressed in a form of satisfying the constructive interference condition:

$$\begin{aligned} E_F &= \tau A_\sigma \frac{|C_1|}{\sqrt{l_1/2}} e^{i[\phi_\sigma + k_{\text{SPW}} \cdot r_1 + \text{ang}(C_1)]} \\ &\cdot \left\{ 1 + \sum_2^j \frac{|C_j|/|C_1|}{\sqrt{l_j/l_1}} e^{i[k_{\text{SPW}} \cdot (r_j - r_1) + \text{ang}(C_j/C_1)]} \right\} \\ &= j\tau A_\sigma \frac{|C_1|}{\sqrt{l_1/2}} e^{i[\phi_\sigma + k_{\text{SPW}} \cdot r_1 + \text{ang}(C_1)]}, \end{aligned} \quad (7)$$

where the first arc $j = 1$ is set as a reference. When the geometries of the different arcs satisfy Eq. (7), a good focusing can be obtained at a certain frequency.

As illustrated in Eq. (5), the geometry of slits in the different arcs related to C_j determines its operating band, which stems from the resonance-determined local controlling ability of slits over the phase, amplitude, and dispersion of the SPW field. For a certain geometry of slit arrays, the operating band is very narrow. Figure 1(c) shows the simulated and experimental transmission spectra of slits with four geometry sizes [as illustrated in Appendix A, Fig. 7(a)] for the polarization direction perpendicular to the slit long-axis (i.e., $|E_y|^2$ spectra). The numerical simulation methods can be found in Appendix B. The results show the typical extraordinary optical transmission (EOT) peaks of THz subwavelength metallic hole arrays, which are closely related to SP excitation. The central excitation frequency of SPW is always located slightly higher than the peak frequency of EOT. The dashed line marks the four different SPW excitation frequencies from 0.38 to 0.61 THz with different slit geometries.

When we design these four kinds of slits in different arcs, each arc excites the SPWs at the corresponding frequency and contributes to broadening the frequency band, so the broadband APSR is designed as shown in Fig. 1(b). In particular, the radius r_j of multi-APSRs should be tailored according to the different dispersion characteristics of slits based on Eq. (6). As a comparison, the narrowband APSR including only one kind of slit is also designed, where $\Delta r = n\lambda_{\text{SPW}}$ for $\Delta C_j = 0$. The detailed geometric parameters can be found in Appendix A. In the broadband APSR, the near-field E_z distributions of SPWs excited by each APSR at four different frequencies are simulated as shown in Fig. 1(d), where the temporal and spatial dispersion characteristics among the different APSRs can be seen clearly. The arc radii r_j ($j = \pm 5, \pm 4, \pm 3$, both ± 2 and ± 1) of broadband APSR are precisely designed: (i) for a certain arc, the focusing intensity of SPWs at the

frequency matching its slit size is enhanced; (ii) at a certain frequency, the total phase difference of SPWs excited by multiple APSRs at the focal spot is close to 0 rad, which satisfies the phase matching condition. Furthermore, Fig. 1(e) gives a more comprehensive view of phase distribution, which further proves the theoretical analysis that phase matching at the focal spot has been achieved. Thus, the broadband APSR focuses the SPWs with spin-selectivity to the left and right arc centers over a wider frequency band.

B. Device Fabrication

LC is introduced into the broadband APSR to construct an active on-chip SP metadvice, as shown in Fig. 2(a). The integration of the LC provides an effective strategy for active modulation of the focusing SPWs. The thickness of the LC layer is designed to get an anisotropic phase difference of $\pi/2$ rad at the central frequency of 0.475 THz, which enables the polarization conversion as a quarter-wave plate (QWP). As shown in Fig. 2(b), when the polarization direction of the incident linearly polarized (LP) wave is along $+45^\circ$, the THz wave transmitting through the LC will be converted into an RCP or LCP state in the condition of $\alpha = 0^\circ$ or 90° , respectively, where α represents the angle between the orientation of LC molecules and the x -axis [43]. It is noted that the ratio of LCP and RCP components can be tuned by the rotation of LC molecules. More importantly, the focusing SPW energy distribution of broadband APSR is relevant to the LC orientation, which concentrates at the left or right focal spot when $\alpha = 0^\circ$ or 90° . Therefore, the active modulation of the focusing SPWs can be realized with the rotation of LC molecules driven by the electric field.

The structure of the LC-integrated on-chip metadvice is listed as follows: (i) Broadband APSR, which is fabricated by

a laser direct writing process on gold film with ion sputtering thickness $h_1 = 100$ nm. (ii) The front glass layer, which is the substrate of the broadband APSR. (iii) The LC layer, with its thickness h_3 of 525 μm . LC is filled in the cell between two glass substrates encapsulated by the ultraviolet glue. The LC used in this work is a kind of high-birefringence nematic LC (HTD028200) from Jiangsu Hecheng Technology Co., Ltd., of which n_e and n_o are 1.89 and 1.61 in the THz regime, respectively, that is, its birefringence $\Delta n = 0.28$. It has good thermal stability in the nematic state, and the transition temperatures from solid to nematic state and from nematic state to isotropic state are $T_{SN} = -30^\circ\text{C}$ and $T_{SI} = 103^\circ\text{C}$. The measured THz optical responses of the LC layer are shown in Appendix C. (iv) The back glass substrate, which is a pre-oriented anchor layer in the y direction, so that LC molecules are initially oriented along the y -axis. The thickness of these two JGS1 glass substrates is the same of $h_2 = h_4 = 300$ μm . (v) Two custom copper wires with a diameter of 525 μm , serving as a spacer to ensure the thickness of the LC layer, and also as the electrodes, supporting a biased electric field along the x direction. As the bias electric field increases from 0 to 12 V/mm, the orientation of LC molecules rotates from the y -axis to the x -axis.

C. Experimental Setup

We conduct our experiments by using a near-field scanning THz time-domain spectroscopy (NFS-THz-TDS) system in Figs. 2(c) and 2(d). The excitation source is a femtosecond laser with 780 nm wavelength (CFL-10RFF, from Carmel Laser Company). It works with a repetition rate of 80 MHz, a pulse width of 86 fs, and a maximum average output power of 1.0 W. All experiments were carried out at room temperature (20°C) and relative humidity $<30\%$. The laser beam is divided into

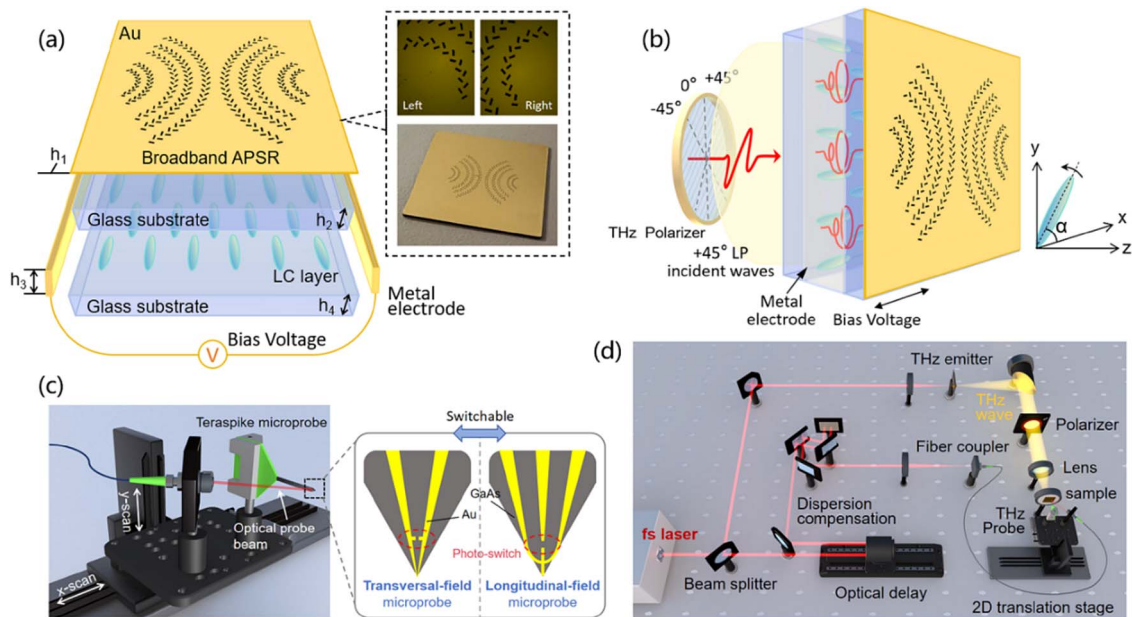


Fig. 2. (a) Structure of THz LC-integrated APSR on-chip metadvice. The photo of practical broadband APSR and its micrographs are shown in the right dotted frame. (b) Schematic diagram of the working principle of LC-integrated SP metadvice. (c) Near-field scanning with THz microprobe. The details of two microprobe types for transversal and longitudinal near-field detection are shown on the right. The antenna gap directions in probe spikes are along the y direction and the z direction. (d) Near-field scanning-terahertz time-domain spectroscopy (NFS-THz-TDS) system.

two optical paths; one is used to generate the THz wave by a GaAs photoconductive antenna, and the other is coupled into an optical fiber and then guides the output beam to the photoconductive near-field probe for THz detection. The sample is placed slightly away from the lens focus so that a parallel THz beam with a diameter of 2 cm is incident on the device from its substrate. The microprobe is fixed on the two-dimensional translation platform to allow mapping of the near-field distribution. In particular, as shown in Fig. 2(c), two types of microprobes, the transversal field microprobe and longitudinal field microprobe (TeraSpike TD-800-X and TD-800-Z, from Proteomics Company, Aachen, Germany), are capable of detecting near-field components of E_y and E_z , respectively. The microprobe is 100 μm away from the device surface. The scanning area is $[-6, +6]$ mm in the x direction and $[-4, +4]$ mm in the y direction with the scanning step of both 1 mm. The mapping pixels after the interpolation algorithm are 61×41 . The time sampling interval is 0.2 ps, and the whole time of each time-domain signal is 40 ps in experiments. Fourier transform is performed with the rectangular window function after padding 0 to 400 ps to obtain the spectrum at each spatial point.

3. RESULTS AND DISCUSSION

A. Broadband SP and Spin-Selective Unidirectional Focusing

To characterize broadband and actively tunable SPWs focusing on devices, both the transversal near field and the longitudinal near field are detected. The transversal component E_y reflects the localized field signal directly through the slits at the SPW excitation position, and the longitudinal component E_z just reflects the SPW propagation on the metallic surface. First, the normalized transmittance spectra of near-field E_y at several key scanning points labeled P_1 – P_8 on the broadband APSR are obtained, as shown in Fig. 3(a). We notice that there is an EOT peak appearing at about 0.6 THz, 0.5 THz, 0.4 THz,

and 0.35 THz, as the corresponding detected positions spatially move from P_1 to P_4 and mirrors from P_8 to P_5 . The experimental results indicate that the central frequency to excite SPWs of each arc in APSR is different, on account of the corresponding slits being different in size. The peak frequency of the near field on the whole APSR structure is in good agreement with that of far-field results in Fig. 1(c). Meanwhile, Figs. 3(b) and 3(c) illustrate that near-field E_y hot spots are mainly concentrated on slits among the arcs numbered $[\pm 5, \pm 4]$, $[\pm 3, \pm 2]$, and $[\pm 1]$, respectively, at 0.35, 0.475, and 0.60 THz, while being weak at the remaining part of the structure due to total metal reflection. It is preliminarily indicated that the SPWs of different frequencies are excited by the arc of different radii in the broadband APSR as predicted in the theoretical design in Section 2.

Next, we investigate the longitudinal near-field E_z component to directly demonstrate the broadband SPW focusing characteristics of the broadband APSR. The LCP and RCP waves are normally incident on the chip surface to obtain the two different output states since the focusing of the SPWs on each side is spin-dependent. A THz QWP is applied in the experiment to convert the LP wave into the CP waves in the NFS-THz-TDS experiment, of which details can be found in Appendix D.

Figure 4(a) shows the near-field E_z transmission spectra at the focal spot for the focusing and defocusing states on the broadband and the narrowband APSR, respectively. Since the mirror-symmetric pattern of APSR makes the unidirectional focusing, that is, when a strong focusing of the SPW occurs around the center of one side, the SPWs defocus on the other side with the maximum extinction ratio of 25 dB for the broadband APSR and 20 dB for the narrowband APSR. As the 5 dB bandwidth is considered as an index, it shows that the operating bandwidth of the broadband APSR is 270 GHz in the range of 0.33–0.60 THz, which is significantly broader by 2.45 times than the narrowband APSR within 110 GHz, from 0.45 to 0.56 THz. Figures 4(b) and 4(c) illustrate the simulated and experimental near-field SPW intensity ($|E_z|^2$) distributions under LCP incidence. Obviously, at 0.475 THz, the SPWs excited on both the broadband and narrowband APSR propagate unidirectionally to the left and focus at the left center. The difference is that the focusing state still maintains at 0.35 THz and 0.60 THz in the broadband APSR, but not in the narrowband APSR. Similarly, the SPWs focus unidirectionally on the right center under RCP incidence, as additionally shown in Fig. 9(c) (Appendix D).

To evaluate the focusing performance, the resolution of the focal spot is defined as

$$R = S_{\text{FWHM}}/\lambda_0, \quad (8)$$

where S_{FWHM} represents the spot diameter with half of the focusing peak, and λ_0 is the wavelength in free space. We choose the central frequency of 0.475 THz to discuss the SPW focusing resolution and its free-space wavelength $\lambda_0 = 631 \mu\text{m}$ ($\lambda_{\text{SPW}} < \lambda_0$). In the simulation, as shown in Figs. 4(d) and 4(e), the focusing resolutions of the broadband and narrowband APSRs are approximately the same, which indicates that the broadband design eliminates the spatial dispersion well and does not cause deterioration of the focusing resolution. The

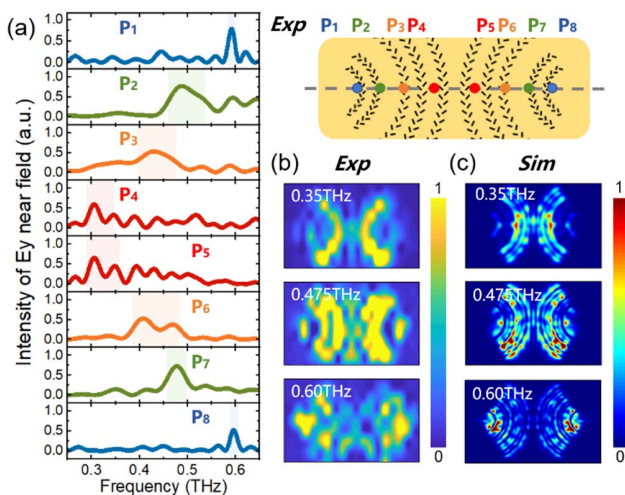


Fig. 3. Transversal near-field detection on the broadband APSR. (a) Normalized transmittance spectra of E_y components in the near field of broadband APSR at the scanning points from P_1 to P_8 . (b) Experimental and (c) simulated near-field E_y component intensity distributions.

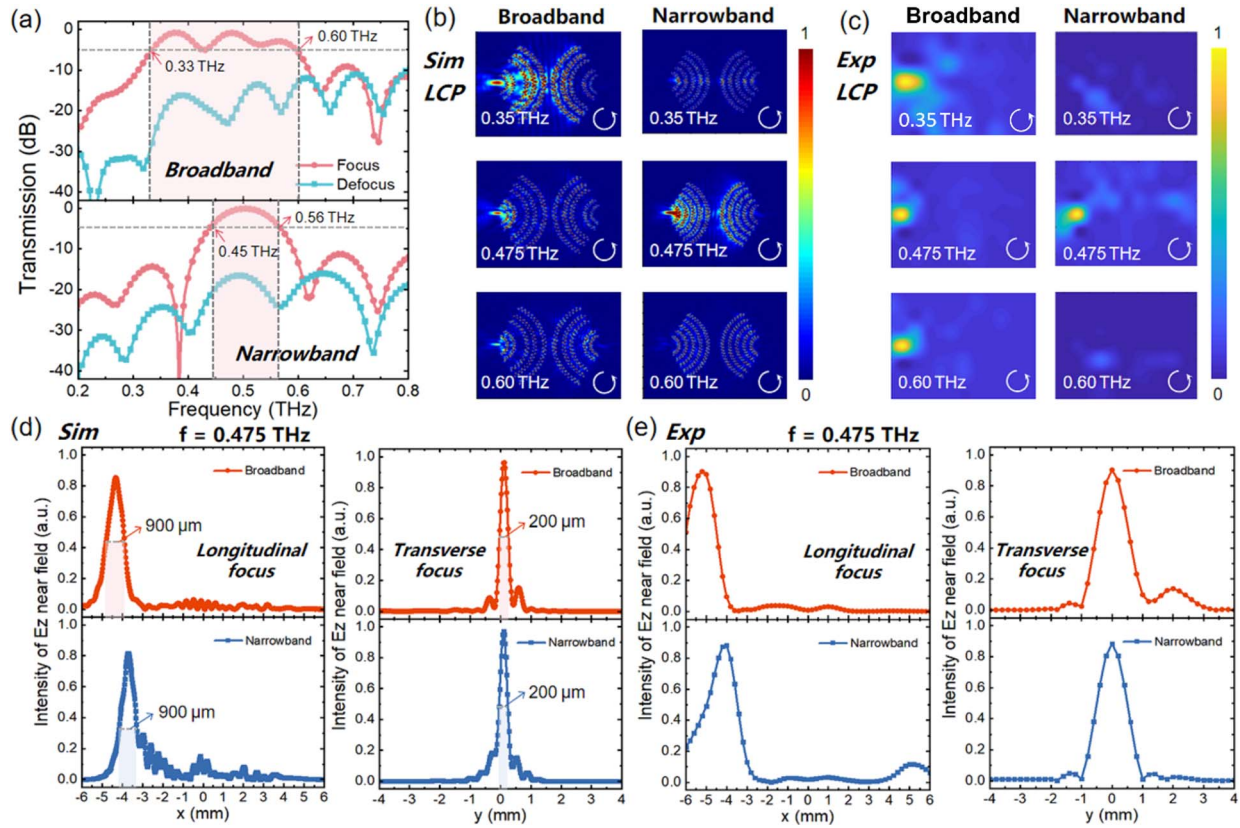


Fig. 4. Longitudinal near-field detection of the APSR. (a) Near-field E_z spectra of broadband and narrowband APSR in focusing and defocusing cases. (b) The simulated near-field E_z intensity distributions of the broadband and narrowband APSR under the LCP incidence. (c) The corresponding experimental results. (d) The simulated near-field E_z intensity distributions of the longitudinal focusing along the x direction and the transverse focusing along the y direction on the focal spot at 0.475 THz. (e) The corresponding experimental results.

transverse resolution is $0.32\lambda_0$, higher than the longitudinal resolution of $1.42\lambda_0$ in the simulation. The experimental results are lower than those in simulations. This is caused by the limitation of the probe scanning precision and the increase of the distance between the probe and the metallic surface in the experiment to limit the scanning time and prevent probe damage. Therefore, a broadband spin-dependent unidirectional SPW transmission is achieved in the broadband APSR, of which the mirror-symmetric structure makes it selectively focus to one side according to the incident spin state.

B. Active Unidirectional Focusing of the SPW

In this part, we demonstrate the LC-integrated APSR on-chip metadvice by the near-field E_z intensity distributions. As shown in Fig. 5(a), the LC orientation can be controlled dynamically with the external electric bias in the x - y plane. When there is no external electric field, the LC molecules are pre-oriented along the y -axis and most of the SPW is concentrated around the left focal spot. With the increase of the external electric field, the LC gradually rotates towards the x -axis, and the SPW energy is distributed in a certain proportion between both sides. Once the external electric field reaches 12 V/mm, the LC molecules are completely oriented along the x -axis, so that the SPWs focus on the right center. Figures 5(b) and 5(c) show the SPWs focus on the left at 0 V/mm and then

turn to the right at 12 V/mm at 0.35, 0.45, and 0.55 THz, and the simulated results are consistent with the experimental measurements.

A measured time-domain signal at the left focal spot is displayed in Fig. 5(d) in focusing and defocusing cases, and the corresponding frequency-domain spectra are obtained in Fig. 5(e) after data processing. It is indicated that active unidirectional on-chip focusing is achieved in the range of 0.33–0.60 THz, with an extinction ratio up to 20 dB. Figures 5(f) and 5(g) present the near-field E_z intensity distributions along the x -cutting line through the focal spots to characterize the spatial dispersion of the SPW focusing in the broadband range. The relative offset rate D of the one-side focal spot is defined to describe the achromatic focusing ability, and its calculation formula is as follows:

$$D = A/S_{\text{FWHM}}, \quad (9)$$

where A stands for the absolute offset distance of the focused spot, and S_{FWHM} is the spot diameter at the central frequency of f_0 . Thus, $D_{\text{horizontal}} = 12\%$ with the condition of $A_{\text{horizontal}} = 125 \mu\text{m}$ and $f_0 = 0.45 \text{ THz}$. These results show that the SPWs of different frequencies are focused on the same point, indicating the device design eliminates the spatial dispersion of wideband focusing.

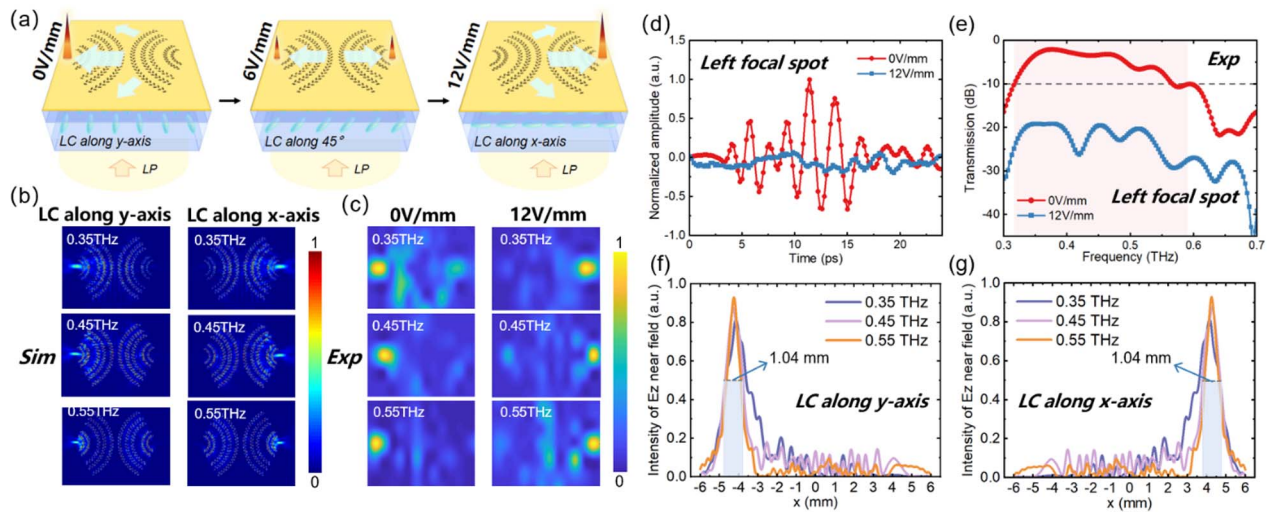


Fig. 5. (a) Diagram of active energy distribution in the LC-integrated broadband APSR on-chip metadvice. (b) Simulated and (c) experimental near-field E_z intensity distributions for active unidirectional focusing of SPWs when the LC is oriented along the y -axis (0 V/mm) and x -axis (12 V/mm). (d) Measured time-domain signals at the left focal spot under the electric field of 0 V/mm and 12 V/mm. (e) Experimental near-field E_z spectra of LC-integrated broadband metadvice in focusing and defocusing cases. x -cutting line through the focal spots when the LC orientation is along (f) the y -axis and (g) the x -axis.

Finally, the active modulation and energy distribution processes of the THz SPWs are demonstrated. As shown in Figs. 6(a) and 6(b), the LC orientation angle α is set varying from 90° to 0° to model the process of applying electric bias in the experiment. As the bias electric field intensity increases from 0 V/mm to 12 V/mm, the focusing SPWs' intensity on the left center gradually decreases from the "on" to "off" state, and the modulation process on the right side is opposite. To characterize the performance of active modulation, the modulation depth M is defined as follows: $M = (I_{\max} - I_{\min}) / I_{\max}$, where I_{\max} and I_{\min} are the SPW intensity corresponding to the focusing switch on and off, respectively. Figures 6(c) and 6(d) show the variation of transverse focal spot intensity during

the electric modulation and reflect that the introduction of the LC layer does not change the spatial resolution of SPW focusing, compared with Figs. 4(d) and 4(e). The modulation depth in simulation can reach 97.3%, while that in the experiment is slightly lower, achieving 73% driven by the electric field. Therefore, the LC-integrated APSR on-chip metadvice exhibits a high sensitivity for the modulation of SPWs focused in opposite directions, with most energy transferring dynamically.

4. CONCLUSION

In conclusion, we have demonstrated an LC-integrated APSR on-chip metadvice, combining the spin-selective unidirectional focusing of SPW in mirror-symmetric multi-APSR structure and the polarization conversion of LC. A strategy for broadband achromatic focusing is provided in which a variety of slit geometry parameters and corresponding arc radii are elaborately tailored to meet the phase matching. The final focal spot would not deviate from the desired position to achieve achromatic focusing since the excited SPWs arrive at that point in phase. The LC-integrated metadvice realizes the active energy distributions of SPWs between left and right focal spots by applying a biased electric field. Both the simulation and experimental characterization show that the operating bandwidth is 270 GHz of 0.33–0.60 THz, which is significantly widened by 2.45 times compared to that of the narrowband devices. In terms of the on-chip focal spots, the transverse resolution is $0.32\lambda_0$, and the horizontal relative offset is only 12%. In addition, the experimental modulation depth of the SPW focusing can reach up to 73%. With new mechanisms and versatility including the wide operating bandwidth, and directional SPWs' excitation, focusing, and active modulation in a single metadvice, this work paves the way for many exciting possibilities of realistic integrated THz SP on-chip applications.

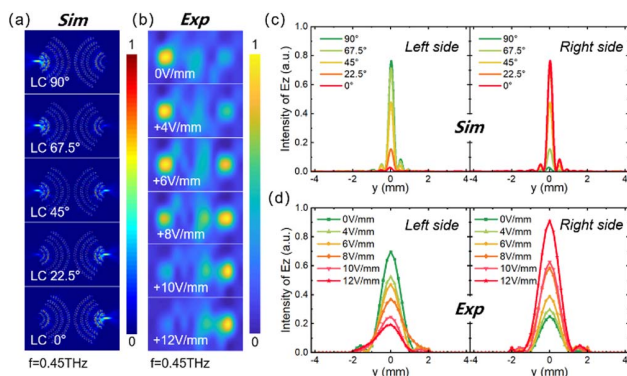


Fig. 6. At 0.45 THz, the near-field E_z intensity distribution with the dynamic modulation of SPWs at the left and right focal spots: (a) as the LC rotates from y - to x -axis in the simulation; (b) as the external electric field is enhanced in the experiment. (c) Simulated and (d) experimental near-field E_z intensity distribution along the y -cutting line through the focal spots on the left and right sides.

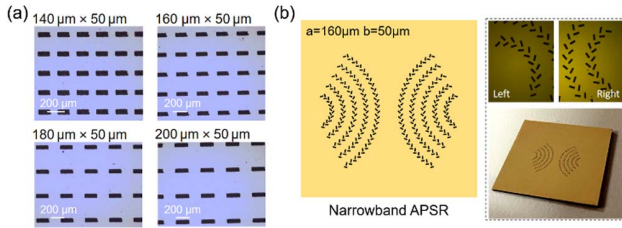


Fig. 7. (a) Optical micrographs of slit array metasurfaces. The geometric sizes of slits are $140 \mu\text{m} \times 50 \mu\text{m}$, $160 \mu\text{m} \times 50 \mu\text{m}$, $180 \mu\text{m} \times 50 \mu\text{m}$, and $200 \mu\text{m} \times 50 \mu\text{m}$. (b) Diagram of narrowband APSR structure. The actual device and optical micrographs are shown on the right.

APPENDIX A: STRUCTURE PARAMETERS OF APSR

A slit can be approximately considered as a dipole source for SPW excitation. To investigate the relation between the slit geometry and the operating frequency to excite SPWs, slit array metasurfaces are constructed. As shown in Fig. 7(a), the slit array metasurfaces with a certain slit size are fabricated by ion-sputtering metallic film and a laser direct writing process on a glass substrate.

The broadband characteristic is confirmed by comparison with common narrowband metadevices with slits in a uniform size. Figure 7(b) illustrates the structural diagram and optical micrographs of narrowband APSR. Each side of the structure is composed of five APSRs with $\psi = 120^\circ$. Specific geometric parameters of the broadband and narrowband APSRs are shown in Tables 1 and 2.

APPENDIX B: NUMERICAL SIMULATION

Numerical simulations are performed by utilizing the finite-difference time-domain (FDTD) method in the commercial software Lumerical FDTD Solution. Boundaries in x , y , and z directions are surrounded by perfectly matched layers. The refractive index of glass is set to 1.9, and the gold can be viewed

Table 1. Geometric Parameters of the Broadband APSR

	$j = \pm 1$	± 2	± 3	± 4	± 5
a_j (μm)	200	200	180	160	140
b_j (μm)	50	50	50	50	50
l_j (μm)	200	200	184	150	120
θ_j ($^\circ$)	5	6	8	10	15
r_j (μm)	4000	3200	2576	1500	960

Table 2. Geometric Parameters of the Narrowband APSR

	$j = \pm 1$	± 2	± 3	± 4	± 5
a_j (μm)			160 for all		
b_j (μm)			50 for all		
l_j (μm)			150 for all		
θ_j ($^\circ$)	5	6	8	10	15
r_j (μm)	3300	2700	2100	1500	900

as a perfect electrical conductor (PEC). The LC layer is modeled as a medium with uniaxial anisotropy, of which the extraordinary and ordinary refractive indices (n_e and n_o) are set to 1.9 and 1.6, respectively. To represent the orientation of the LC molecules, the anisotropic dielectric constant of LC is expressed in a tensor form through a certain orthogonal coordinate transformation from the original diagonal tensor. In this work, the spatial orientation angle is taken by $(90^\circ, \alpha)$ to describe the main axis of LC rotating in the x - y plane, where α represents the angle between the LC orientation and the x -axis. To measure longitudinal and transversal near field, the monitors for E_z and E_y are placed $50 \mu\text{m}$ and $150 \mu\text{m}$ above the metadvice on the air side, respectively. Point monitors are placed around the arc center at each side to detect the intensity transmission spectrum at the focal spot in opposite focusing directions, and a surface monitor placed in the x - y plane with different frequency points is used to obtain corresponding intensity distributions.

APPENDIX C: OPTICAL RESPONSES OF THE LC LAYER

To characterize the optical properties of the LC layer used in this work, an LC cell the same as that in the LC-integrated on-chip metadvice is fabricated. LC molecules are pre-oriented along the y -axis by the anchoring effect of the anchoring layer. In experiments, a 45° -LP wave is incident into the LC cell as mentioned in Section 3.B of the main text, and the $\pm 45^\circ$ orthogonal components of the output time-domain signals are measured by rotating the polarizer behind the sample. In Fig. 8(a), the normal and extraordinary refractive indices (n_o and n_e) of the LC material can reach ~ 1.89 and ~ 1.61 in the frequency range of 0.2–0.8 THz, and the birefringence coefficient (Δn) is about 0.28, which is close to the simulation parameters set above. Figure 8(b) demonstrates the pronounced polarization conversion characteristic of the specific LC layer. It acts as a broadband QWP with a central frequency of 0.51 THz. The polarization conversion extinction between two outgoing orthogonal circularly polarized states is more than 10 dB on average in the frequency band of 0.31–0.66 THz.

APPENDIX D: SUPPLEMENTARY RESULTS OF APSR

According to Fig. 4(a) of the main text, for the APSR structure, when the incident wave is CP, the near-field E_z transmission at the arc center of one side is higher than that at the other side. The near-field E_z intensity extinction ratio is used to evaluate

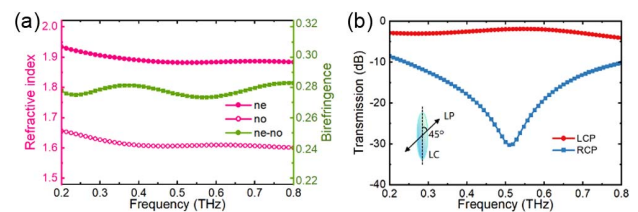


Fig. 8. (a) Normal refractive index n_o and extraordinary refractive index n_e of LC and its birefringence coefficient. (b) Experimental polarization conversion spectra of the LC layer from a 45° -LP to LCP state.

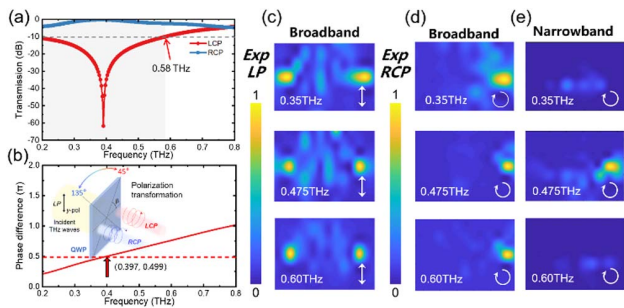


Fig. 9. (a) Transmission and (b) phase spectrum of QWP. The diagram illustrates the polarization conversion characteristics varying with the angle β by the mechanical rotation of its fast-axis. (c) Near-field E_z distribution on broadband APSR under LP incidence and (d) under RCP incidence, and that on (e) narrowband APSR under RCP incidence, at 0.35, 0.475, and 0.60 THz.

the effect of spin-selective unidirectional SPW focusing. The calculation formula is as follows:

$$E_{xt} = 10 \log(I_{\text{Focus}}/I_{\text{Defocus}}). \quad (\text{D1})$$

The maximum extinction ratio of broadband APSR is 25 dB in the frequency range of 0.33–0.60 THz, and that of narrowband APSR is 20 dB within 0.45–0.56 THz. The results show that the APSR structure can achieve a good unidirectional SPW focusing effect.

To characterize the spin-selective unidirectional focusing characteristics of SPW in APSR, experiments require the CP THz waves as the incidence. In addition, the bandwidth characteristics of APSR need to be verified. A QWP is placed between the lens and the sample, of which the orientation is described by the angle β between the fast-axis and the x -axis. As shown in Figs. 9(a) and 9(b), the y -polarized incidence LP wave will be converted into the LCP state when $\beta = +45^\circ$ and into an RCP state when $\beta = +135^\circ$. Besides, it serves as a perfect QWP at 0.397 THz. Moreover, this QWP exhibits good spin-state conversion effects over a wide frequency range of 0.2–0.58 THz.

Figures 9(d) and 9(e) supplementarily show the RCP-dependent SPW focusing on the right side excited by two types of APSRs within the wideband and narrowband, respectively. At 0.35, 0.475, and 0.60 THz, SPWs maintain the unidirectional focusing state around the right center of wideband APSR. For narrowband APSR, SPWs are only focused at 0.475 THz, while shown unfocused at the other two frequencies. Additionally, when an LP wave is incident in the APSR device, which can be regarded as a synthesis of the LCP and RCP waves with equal components, SPWs will focus at both left and right focal spots with the same energy. Therefore, it is clarified that not only the spin-selective unidirectional focusing of SPWs is excited by APSR structure, but also the widened operating bandwidth of the broadband APSR compared with narrowband devices.

Funding. National Natural Science Foundation of China (62205160, 62235004, 62335012, 62371258); Fundamental Research Funds for the Central Universities (Nankai University) (63241330).

Disclosures. The authors declare no conflicts of interest.

Data Availability. Data underlying the results presented in this paper are not publicly available at this time but may be obtained from the authors upon reasonable request.

REFERENCES

- J. J. Ma, R. Shrestha, J. Adelberg, *et al.*, "Security and eavesdropping in terahertz wireless links," *Nature* **563**, 89–93 (2018).
- W. N. Shi, Y. M. Wang, F. Fan, *et al.*, "THz enantiomers of drugs recognized by the polarization enhancement of gold nanoparticles on an asymmetric metasurface," *Nanoscale* **15**, 14146–14154 (2023).
- Y. Zhu, B. B. Lu, Z. Y. Fan, *et al.*, "Geometric metasurface for polarization synthesis and multidimensional multiplexing of terahertz converged vortices," *Photon. Res.* **10**, 1517–1532 (2022).
- X. F. Zang, H. Z. Ding, Y. Intaravanne, *et al.*, "A multi-foci metalens with polarization-rotated focal points," *Laser Photon. Rev.* **13**, 1900182 (2019).
- B. W. Sun, X. F. Zang, B. B. Lu, *et al.*, "Generalized terahertz perfect vortices with transmutable intensity profiles based on spin-decoupled geometric metasurfaces," *Adv. Opt. Mater.* **11**, 2301048 (2023).
- W. L. Barnes, A. Dereux, T. W. Ebbesen, *et al.*, "Surface plasmon sub-wavelength optics," *Nature* **424**, 824–830 (2003).
- Y. Fang and M. Sun, "Nanoplasmonic waveguides: towards applications in integrated nanophotonic circuits," *Light Sci. Appl.* **4**, e294 (2015).
- F. J. Garcia-Vidal, A. I. Fernández-Domínguez, L. Martín-Moreno, *et al.*, "Spoof surface plasmon photonics," *Rev. Mod. Phys.* **94**, 025004 (2022).
- Q. Xu, Y. Lang, X. Jiang, *et al.*, "Meta-optics inspired surface plasmon devices," *Photon. Insights* **2**, R02 (2023).
- X. Zhang, Q. Xu, L. Xia, *et al.*, "Terahertz surface plasmonic waves: a review," *Adv. Photon.* **2**, 014001 (2020).
- X. F. Zang, Y. M. Zhu, C. X. Mao, *et al.*, "Manipulating terahertz plasmonic vortex based on geometric and dynamic phase," *Adv. Opt. Mater.* **7**, 1801328 (2019).
- X. Zhang, Y. Xu, W. Yue, *et al.*, "Anomalous surface wave launching by handedness phase control," *Adv. Mater.* **27**, 7123–7129 (2015).
- L. Y. Lee, K. Kim, S. J. Kim, *et al.*, "Plasmonic meta-slit: shaping and controlling near-field focus," *Optica* **2**, 6–13 (2015).
- X. Su, Q. Xu, Y. Lu, *et al.*, "Gradient index devices for terahertz spoof surface plasmon polaritons," *ACS Photon.* **7**, 3305–3312 (2020).
- F. Liu, D. Wang, H. Zhu, *et al.*, "High-efficiency metasurface-based surface-plasmon lenses," *Laser Photon. Rev.* **17**, 2201001 (2023).
- J. Lin, J. P. B. Mueller, Q. Wang, *et al.*, "Polarization-controlled tunable directional coupling of surface," *Science* **340**, 331–334 (2013).
- X. Jiang, Q. Xu, Y. Lang, *et al.*, "Geometric phase control of surface plasmons by dipole sources," *Laser Photon. Rev.* **17**, 2200948 (2023).
- Q. Xu, X. Zhang, Q. Yang, *et al.*, "Polarization-controlled asymmetric excitation of surface plasmons," *Optica* **4**, 1044–1051 (2017).
- Z. Wang, S. Li, X. Zhang, *et al.*, "Excite spoof surface plasmons with tailored wavefronts using high-efficiency terahertz metasurfaces," *Adv. Sci.* **7**, 2000982 (2020).
- J. Han, Y. Xu, H. Zhang, *et al.*, "Functional meta lenses for compound plasmonic vortex field generation and control," *Adv. Funct. Mater.* **32**, 2111000 (2022).
- E. Prinz, G. Spektor, M. Hartelt, *et al.*, "Tailorable polarization-dependent directional coupling of surface plasmons," *Nano Lett.* **21**, 3941–3946 (2021).
- Y. Lang, Q. Xu, X. Chen, *et al.*, "On-chip plasmonic vortex interferometers," *Laser Photon. Rev.* **16**, 2200242 (2022).
- C. H. Gan and G. R. Nash, "Broadband and efficient plasmonic control in the near-infrared and visible via strong interference of surface plasmon polaritons," *Opt. Lett.* **38**, 4453–4456 (2013).
- B. Chen, J. Yang, C. Hu, *et al.*, "Plasmonic polarization nano-splitter based on asymmetric optical slot antenna pairs," *Opt. Lett.* **41**, 4931–4934 (2016).

25. M. Feng, B. Zhang, H. Ling, *et al.*, "Active metal-graphene hybrid terahertz surface plasmon polaritons," *Nanophotonics* **11**, 3331–3338 (2022).
26. H. Su, Q. Li, G. Xu, *et al.*, "Active control of polarization-dependent terahertz surface plasmonic wave excitation using coupled graphene-metal hybrid metasurfaces," *Phys. Scr.* **99**, 025526 (2024).
27. Q. Li, H. Su, G. Xu, *et al.*, "Active control of terahertz surface plasmonic wave excitation using electromagnetically induced transparency based graphene metasurfaces," *Opt. Express* **31**, 37452–37463 (2023).
28. L. Chen, T. Ren, Y. Zhao, *et al.*, "Polarization-independent wavefront manipulation of surface plasmons with plasmonic metasurfaces," *Adv. Opt. Mater.* **8**, 2000868 (2020).
29. X. Zhao, X. Feng, P. Zhao, *et al.*, "Polarization-controllably launching localized cosine-Gauss beam with spatially varied metallic nano-apertures," *Opt. Express* **27**, 22053–22073 (2019).
30. L. Zhu, Z. Xiong, W. Yu, *et al.*, "Polarization-controlled tunable multifocal plasmonic lens," *Plasmonics* **12**, 33–38 (2017).
31. M. A. Babil, Z. Zhou, and Q. Deng, "Active unidirectional propagation of surface plasmons at subwavelength slits," *Opt. Express* **21**, 17066–17076 (2013).
32. C. Liu, Y. Xu, R. Huang, *et al.*, "Terahertz metamaterials for broadband, high modulation depth modulator, and tunable dual-band absorber based on metal-vanadium dioxide hybrid structure," *AIP Adv.* **13**, 095204 (2023).
33. J. Li, J. Li, C. Zheng, *et al.*, "Dynamic control of reflective chiral terahertz metasurface with a new application developing in full grayscale near field imaging," *Carbon* **172**, 189–199 (2021).
34. J. T. Li, J. Li, C. Zheng, *et al.*, "Active controllable spin-selective terahertz asymmetric transmission based on all-silicon metasurfaces," *Appl. Phys. Lett.* **118**, 221110 (2021).
35. Y. Sun, Y. Xu, H. Li, *et al.*, "Flexible control of broadband polarization in a spintronic terahertz emitter integrated with liquid crystal and metasurface," *ACS Appl. Mater. Interfaces* **14**, 32646–32656 (2022).
36. O. Buchnev, N. Podoliak, K. Kaltenecker, *et al.*, "Metasurface-based optical liquid crystal cell as an ultrathin spatial phasmodulator for THz applications," *ACS Photon.* **7**, 3199–3206 (2020).
37. M. A. Naveed, J. Kim, I. Javed, *et al.*, "Novel spin-decoupling strategy in liquid crystal-integrated metasurfaces for interactive metadisplays," *Adv. Opt. Mater.* **10**, 2200196 (2022).
38. H. J. Zhao, F. Fan, T. R. Zhang, *et al.*, "Dynamic terahertz anisotropy and chirality enhancement in liquid-crystal anisotropic dielectric metasurfaces," *Photon. Res.* **10**, 1097–1106 (2022).
39. C. X. Liu, F. Yang, J. F. Xiao, *et al.*, "Programmable manipulations of terahertz beams by transmissive digital coding metasurfaces based on liquid crystals," *Adv. Opt. Mater.* **9**, 2100932 (2021).
40. X. Zhuang, W. Zhang, K. Wang, *et al.*, "Active terahertz beam steering based on mechanical deformation of liquid crystal elastomer metasurface," *Light Sci. Appl.* **12**, 14 (2023).
41. X. Fu, L. Shi, J. Yang, *et al.*, "Flexible terahertz beam manipulations based on liquid-crystal-integrated programmable metasurfaces," *ACS Appl. Mater. Interfaces* **14**, 22287–22294 (2022).
42. T. V. Teperik, A. Archambault, F. Marquier, *et al.*, "Huygens-Fresnel principle for surface plasmons," *Opt. Express* **17**, 17483–17490 (2009).
43. J. Liu, F. Fan, Z. Tan, *et al.*, "Terahertz cascaded metasurfaces for both spin-symmetric and asymmetric beam diffractions with active power distribution," *APL Photon.* **8**, 096112 (2023).